Design and optimization of hole collectors based on nc-SiO_x:H for high-efficiency silicon heterojunction solar cells

Zhao, Yifeng; Procel, Paul; Han, Can; Mazzarella, Luana; Yang, Guangtao; Weeber, Arthur; Zeman, Miro; Isabella, Olindo

DOI
10.1016/j.solmat.2020.110779

Publication date
2021

Document Version
Final published version

Published in
Solar Energy Materials and Solar Cells

Solar Energy Materials & Solar Cells 219 (2021) 110779

Contents lists available at ScienceDirect

Solar Energy Materials and Solar Cells

journal homepage: http://www.elsevier.com/locate/solmat

Design and optimization of hole collectors based on nc-SiO$_x$:H for high-efficiency silicon heterojunction solar cells

Yifeng Zhao [a,*], Paul Procel [a], Can Han [a,b], Luana Mazzarella [a], Guangtao Yang [a], Arthur Weeber [a,c], Miro Zeman [a], Olindo Isabella [a]

[a] Photovoltaic Materials and Devices Group, Delft University of Technology, Delft, the Netherlands
[b] Shenzhen Institute of Wide-Bandgap Semiconductors, Shenzhen, PR China
[c] TNO Energy Transition, Solar Energy, Petten, the Netherlands

ARTICLE INFO

Keywords:
Silicon heterojunction (SHJ)
Hydrogenated nanocrystalline silicon oxide (nc-SiO$_x$:H)
Optoelectrical properties
Interface treatment
Contact resistivity (ρ_c)
Activation energy (E_a)

ABSTRACT

Low activation energy (E_a) and wide bandgap (E_g) are essential for (*p*)-contacts to achieve effective hole collection in silicon heterojunction (SHJ) solar cells. In this work, we study Plasma-Enhanced Chemical Vapor Deposition *p*-type hydrogenated nanocrystalline silicon oxide, (*p*)nc-SiO$_x$:H, combined with (*p*)nc-Si:H as (*p*)-contact in front/back-contacted SHJ solar cells. We firstly determine the effect of a plasma treatment at the (*i*)a-Si:H/(*p*)-contact interface on the thickness-dependent E_a of (*p*)-contacts. Notably, when the (*p*)nc-Si:H layer is thinner than 20 nm, the E_a decreases by applying a hydrogen plasma treatment and a very-high-frequency (*i*)nc-Si:H treatment. Such an interface treatment also significantly reduces the contact resistivity of the (*p*)-contact stacks ($\rho_{c,p}$), resulting in an improvement of 6.1%$_{abs}$ in fill factor (*FF*) of the completed cells. Thinning down the (*i*)a-Si:H passivating layer to 5 nm leads to a low $\rho_{c,p}$ (144 mΩ·cm^2) for (*p*)-contact stacks. Interestingly, we observe an increment of *FF* from 72.9% to 78.3% by using (*p*)nc-SiO$_x$:H layers featuring larger differences between their optical gap (E_{04}) and E_a, which tend to enhance the built-in potential at the c-Si/(*i*)a-Si:H interface. Furthermore, we observe clear impacts on $\rho_{c,p}$, open-circuit voltage, and *FF* by optimizing the thicknesses of (*p*)-contact that influence its E_a. In front junction cells, the vertical and lateral collection of holes is affected by $\rho_{c,p}$ of (*p*)-contact stacks. This observation is also supported by TCAD simulations which reveal different components of lateral contributions. Lastly, we obtain both front and rear junction cells with certified *FF* well-above 80% and the best efficiency of 22.47%.

1. Introduction

Front/back-contacted silicon heterojunction (FBC-SHJ) solar cells with carrier-selective passivating contacts based on hydrogenated amorphous silicon (a-Si:H) achieved conversion efficiency well-above 25% [1]. However, the application of (*p*)a-Si:H for hole collection is challenging because of its high parasitic absorption [2] and moderate doping efficiency [3–5]. The latter imposes constraints on the energy alignment for charge carrier transport from c-Si bulk to the indium tin oxide (ITO) transparent conductive oxide (TCO), thus limiting the device fill factor (*FF*) and open-circuit voltage (V_{oc}) [6–11]. A theoretical study performed by our group [10] suggests that an efficient (*p*)-contact needs to exhibit wide bandgap (E_g) and low activation energy (E_a) for improving the junction built-in voltage (V_{bi}), thus improving the selectivity for holes. Specifically, we assume a heterostructure that consists of a (*n*)c-Si substrate and a (*p*)-type layer. For simplicity, we neglect the (*i*)-type layer in between the (*n*)c-Si and the (*p*)-type layer. Under thermal equilibrium, the band bending at (*n*)c-Si/(*p*)-type layer interface is indicated by the V_{bi} and it is defined as [10]:

$$V_{bi} = \varphi_p - \varphi_n \tag{1-1}$$

and

$$\varphi_p = \chi_{e,p} + E_{g,p} - E_{a,p} \tag{1–2}$$

with φ_p the work function of the (*p*)-type layer, φ_n the work function for the (*n*)c-Si substrate, $\chi_{e,p}$ the electron affinity of the (*p*)-type layer, $E_{g,p}$ and $E_{a,p}$ the bandgap and activation energy of the (*p*)-type layer, respectively. By substituting equations (1-2) into (1-1), we obtain:

* Corresponding author. Photovoltaic Materials and Devices Group, Delft University of Technology, Mekelweg 4, 2628 CD, Delft, the Netherlands.
E-mail address: Y.Zhao-4@tudelft.nl (Y. Zhao).

https://doi.org/10.1016/j.solmat.2020.110779
Received 31 May 2020; Received in revised form 17 August 2020; Accepted 28 August 2020
Available online 7 September 2020

$$V_{bi} = \chi_{c,p} + E_{g,p} - E_{a,p} - \varphi_n \quad (1–3)$$

Since φ_n is fixed for the (n)c-Si and the $\chi_{c,p}$ is assumed constant for thin-film layers [12], to maximize the V_{bi} (and also c-Si band bending), a maximal $E_{g,p}$ - $E_{a,p}$ is preferred. That is, the requirement for a low $E_{a,p}$ (p)-type layer is relaxed if the layer also features a higher $E_{g,p}$ [10].

Hydrogenated nanocrystalline silicon oxide (nc-SiO_x:H), featuring tunable and superior optoelectrical properties over standard a-Si:H, has been proposed as carrier-selective passivating contact and implemented in SHJ solar cells [13–29]. Specifically, E_a and E_g of nc-SiO_x:H can be so finely tuned that effective carriers' transport can be achieved. To further improve this hole-selective transport, (p)nc-SiO_x:H and (p)nc-Si:H can be combined in a (p)-contact stack [10]. Indeed, aside from their optical advantages over the standard doped a-Si:H layers [19,28,30], the bi-layer contacts minimize the transport losses by (a) improving the hole accumulation at c-Si/(i)a-Si:H interface with a wide E_g (p)nc-SiO_x:H, and (b) enhancing the charge exchange from (p)-contact to ITO with a low E_a (p)nc-Si:H layer. Due to the substrate-dependent growth characteristics of (p)nc-SiO_x:H [31], prompt nucleation of nanocrystals [28] is required for its implementation into SHJ solar cells featuring an (i)a-Si:H passivation layer, thus achieving a low E_a (p)-contact close to the c-Si/(i) a-Si:H interface.

To provide more insights about the transport mechanisms of charge carriers, efforts have been devoted to investigating the origins of solar cell series resistance (R_{series}), revealing contributions from the bulk of the component materials and their discontinuous interfaces due to different E_g of adjacent materials [32–35]. Among those contributions, doped contact stacks are interesting due to their major contributions to the total device R_{series} [36–40] in terms of contact resistivity (ρ_c). Experimental [41] and theoretical studies [11] reveal close correlations between ρ_c and device's external parameters (*FF* and V_{oc}), where the contact resistivity can be tuned via adjusting the properties of the doped layer (E_a and E_g) and of the TCO layer (carrier concentration, N_e). In other words, manipulation of those electrical properties in bi-layer charge carrier collectors based on (p)nc-SiO_x:H and (p)nc-Si:H determines the alignment of energy states and thus the effectiveness of the charge carrier transport.

In this contribution, we firstly investigate the thickness-dependent E_a of the bi-layer charge carrier collectors based on (p)nc-SiO_x:H and (p)nc-Si:H as function of interfacial treatments [28]. Afterward, we explore the $\rho_{c,p}$ of (p)-contact stacks under varying contacting conditions. Accordingly, we evaluate the effect of $\rho_{c,p}$ on the V_{oc} and *FF* of FBC-SHJ solar cells. To infer the hole transport losses, we decompose the devices' R_{series} in vertical and lateral contributions and we conduct advanced device simulations to understand the lateral collection mechanism of holes in various front junction cell configurations.

2. Methodology

Thin-film silicon layers were deposited in a multi-chamber Plasma-Enhanced Chemical Vapor Deposition (PECVD) system at a frequency of 13.56 MHz or 40.68 MHz with optimized deposition parameters as described in our previous study [28]. Specifically, we present in Table 1 the (p)-contact deposition conditions investigated in this study. To study the effect of interfacial treatments on the thickness-dependent E_a of the (p)-contact, we deposited layers on Corning Eagle XG glass and used spectroscopic ellipsometry (SE) to determine the thicknesses of the deposited films. We determined the optical bandgap (E_{04}) by fitting the measured reflectance and transmittance spectra of the thin-film layers with SCOUT software [42,43]. To extract lateral dark conductivity σ_{dark} and E_a of the doped contacts, we used a temperature-dependent dark current-voltage (I–V) setup. We determined the ρ_c of doped contact stacks by preparing samples with (p)- or (n)-type Topsil float-zone (FZ) <100> c-Si wafers, which are 280 ± 20-μm thick with a resistivity of 3 ± 2 Ω cm, measured with a room-temperature dark I–V setup as introduced elsewhere [44].

Table 1
PECVD parameters for optimization of (p)nc-SiO_x:H, (p)nc-Si:H, HPT, VHF (i)nc-Si:H treatment.

PECVD parameters	(p)nc-SiOx:H	(p)nc-Si:H	HPT	VHF (i)nc-Si:H
Frequency (MHZ)	13.56	13.56	13.56	40.68
Temperature (°C)	180	180	180	180
Pressure (mbar)	1.4–3	2.2	2.2	4
Power density (mW/cm^2)	76	90	63	69
SiH_4 (sccm)	0.8	0.8	/	1.2
H_2 (sccm)	170	170	200	120
CO_2 (sccm)	1.4	0	/	/
B_2H_6 (200 ppm in H_2) (sccm)	10	10	/	/
Deposition rate[a] (nm/s)	0.018–0.036	0.047	/	~0[b]

[a] The deposition rate refers to layers deposited on the flat glass substrates.
[b] The deposition rate is hardly detectable by SE measurement after 6 min of deposition.

For solar cell fabrication, we used the abovementioned 4-inch n-type c-Si wafers as the absorber. We firstly textured the c-Si wafers in diluted tetramethylammonium hydroxide (TMAH) solution with ALKA-TEX as additive [45]. Afterward, we used nitric acid (HNO_3) to clean the textured wafers and diluted hydrofluoric acid (HF) to remove the native oxide layer formed on the surface of the wafers just before loading them into the PECVD [46]. During the PECVD process, we firstly deposited the (i)a-Si:H/(n)-contact, then (i)a-Si:H/(p)-contact on the other side. The interface plasma treatments consisting of a hydrogen plasma treatment and a very high-frequency (VHF) (i)nc-Si:H treatment were applied before the doped contact stack depositions [28]. Subsequently, we applied RF magnetron sputtering system to deposit 75-nm and 150-nm thick indium tin oxide (ITO) on the front and rear side of the solar cell precursors, respectively. Eventually, we screen-printed Ag paste and then cured the printed metal electrodes in an oven with air atmosphere at 170 °C for 45 min. The fabricated solar cells feature a cell area of 3.92 cm^2.

During the fabrication of the solar cells, we tracked the precursor passivation qualities (e.g. implied V_{oc}, i-V_{oc}) before the ITO sputtering by using Sinton WCT-120 with quasi-steady-state photoconductance (QSSPC) or transient photoconductance decay (Transient PCD) mode [47,48]. We characterized the I–V performance of the solar cell by using an AAA class Wacom WXS-156S-L2 solar simulator. Further, for eventually extracting the $R_{s,SunsVoc}$ of the solar cells, we obtained the pseudo-*FF* (*pFF*) and *Suns*V_{OC} from Sinton Suns-V_{OC}-150 Illumination-Voltage Tester. To independently confirm the cell parameters, two cells were measured at the CalTeC of the Institute for Solar Energy Research Hamelin (ISFH), Germany.

Numerical simulations carried out by us are based on TCAD Sentaurus from Synopsys Inc. [49], using experimentally measured geometry, E_a, and E_{04} as input parameters. More details about models and parameters can be found in previous studies [10,11,41]. In this work, we used contact stacks consisting of (i)a-Si:H, (p)nc-SiO_x:H, (p)nc-Si:H, ITO, Ag electrodes as shown in Fig. 1. These layers induce band bending inside the c-Si, which is referred to as the space-charge layer inside the (n) c-Si bulk in this study. A schematic sketch of the band diagram of (p)-contact stack is given in Fig. 1 [10].

3. Results and discussions

3.1. Activation energy of the (p)-contact

Our bi-layer (p)-contact, consisting of (p)nc-SiO_x:H (10 nm) and (p) nc-Si:H (varied thickness), was deposited on a glass substrate coated with (i)a-Si:H (10 nm). This structure is used to take into account the substrate-dependent growth of nc-SiO_x:H thin films in our actual solar cells [31]. We assessed the E_a and σ_{dark} of the (p)-contact with schematic structures given in Fig. 2. To accelerate the nucleation of the (p)nc-SiO_x:

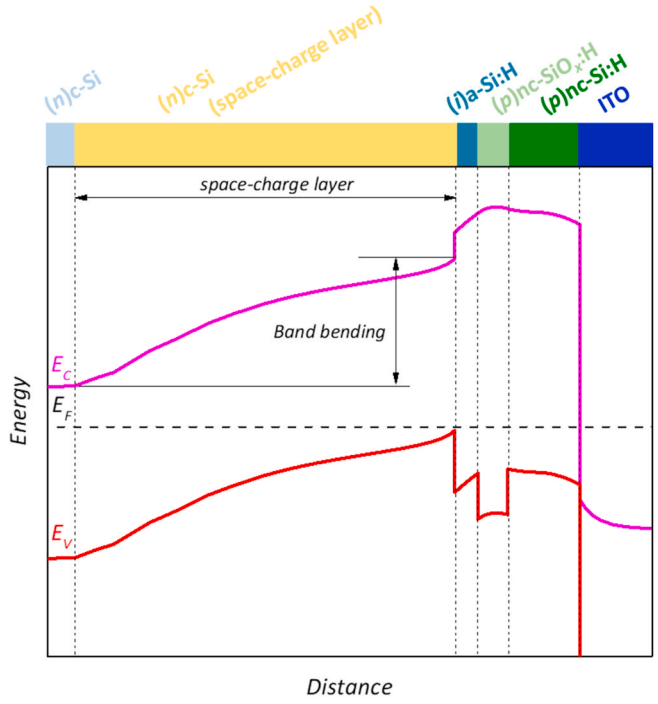

Fig. 1. Schematic sketch (top) and band diagram under the dark thermal equilibrium condition (diagram) of the proposed (*p*)-contact stack for SHJ solar cells with the bi-layer (*p*)-contact. In general, the (*p*)-contact stack consists of a space-charge layer inside the (*n*)c-Si bulk, (*i*)a-Si:H, (*p*)nc-SiO$_x$:H, (*p*)nc-Si:H, ITO, and Ag (not shown here). Figure adapted from Ref. [10].

H, we additionally applied a combined interface treatment including hydrogen plasma treatment (HPT) and very-high-frequency (VHF) (*i*) nc-Si:H treatment (thereafter, simply denoted as *interface treatment*) before the (*p*)-contact deposition, as is proposed in our previous studies [28]. The thickness-dependent E_a and σ_{dark} of (*p*)-contacts with and without interface treatment are illustrated in Fig. 2.

Similar as reported by Cabarrocas et al., [31], E_a decreases and σ_{dark} increases in both types of (*p*)-contacts with increasing (*p*)nc-Si:H thickness and tend to gradual saturation for (*p*)nc-Si:H thicknesses above around 20 nm (see Fig. 2). Besides this general trend, we also observe that the interface treatment induces improvements in electrical properties of (*p*)-contacts, especially, when (*p*)nc-Si:H is thinner than 20 nm. In other words, the interface treatment promotes more conductive layers

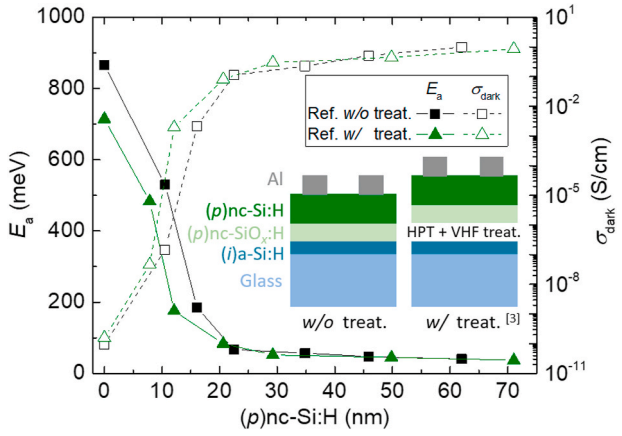

Fig. 2. The influence of interfacial HPT + VHF treatment on E_a and σ_{dark} of bi-layer (*p*)-contact consisting of 10 nm (*p*)nc-SiO$_x$:H and (*p*)nc-Si:H with variable thickness. The schematic structures for assessing E_a and σ_{dark} of the bi-layer (*p*)-contact are also presented.

(lower E_a) and thus potentially a better performing (*p*)-contact for SHJ solar cell applications. Therefore, the interface treatment is chosen to enhance the selective transport of holes [10], because it may result in reduced resistive losses and therefore higher *FF*s in completed solar cells.

3.2. Contact resistivity of the contact stacks

To extract the $\rho_{c,p}$ of the (*p*)-contact stacks in solar cells (see Fig. 3 (a)), we fabricated symmetrical samples (see Fig. 3(b)) featuring the same (*p*)-contact stacks as applied in our solar cells [40]. With R_s, we represent the resistivity with a unit of mΩ·cm^2. Mathematically, for the symmetrical test samples, the total contact resistivity ($R_{s,contacts}$) can be expressed as:

$$R_{s,contacts} = R_{s,sample} - R_{s,bulks} \quad (3\text{-}1)$$

where $R_{s,sample}$ is the total sample resistivity measured directly via the symmetrical sample, $R_{s,bulks}$ is the bulk resistivity contributions from c-Si and thin-film layers that form the doped contact stacks. With known $R_{s,bulks}$, we can extract the $R_{s,contacts}$, which originates from the contact interfaces. Thus, the single-side $\rho_{c,p}$ can be obtained via:

$$\rho_{c,p} = R_{s,contacts}/2 \quad (3\text{-}2)$$

where the term '2' reflects the symmetrical nature of the test sample.

With this methodology, we firstly studied the effects of the interface treatment and thickness of an (*i*)a-Si:H layer on the $\rho_{c,p}$ of the contact stacks. Then, we explored the effects of (*p*)nc-SiO$_x$:H layers that featured different E_{04} and E_a. Lastly, we investigated the $\rho_{c,p}$ by varying the thickness combinations in the bi-layer (*p*)-contact.

3.2.1. Effect of the interface treatment and (i)a-Si:H layer thickness on contact resistivity

To investigate the effect of the interface treatment and the thickness of an (*i*)a-Si:H layer on $\rho_{c,p}$ of the (*p*)-contact stacks, we fabricated symmetrical samples with (*p*)-contact consisting of 4-nm thick (*p*)nc-SiO$_x$:H and 16-nm thick (*p*)nc-Si:H layer. We evaluated carrier transport and passivation quality in terms of $\rho_{c,p}$ of (*p*)-contact stacks and i-V_{oc} of the sample precursor (before ITO sputtering) as shown in Fig. 4 and discussed below.

Looking at the samples with 7-nm thick (*i*)a-Si:H, it is noticeable that the interface treatment significantly reduces the average $\rho_{c,p}$ from 1221 mΩ·cm^2 down to 325 mΩ·cm^2. Since the $\rho_{c,ITO/Ag}$ of ITO/Ag interface is around 1.5 mΩ·cm^2 [50], its contribution is negligible to the total $\rho_{c,p}$ of the contact stack. The reduced $\rho_{c,p}$ reflects the improvement of contacts from c-Si to ITO, which indicates that the interface treatment enables the

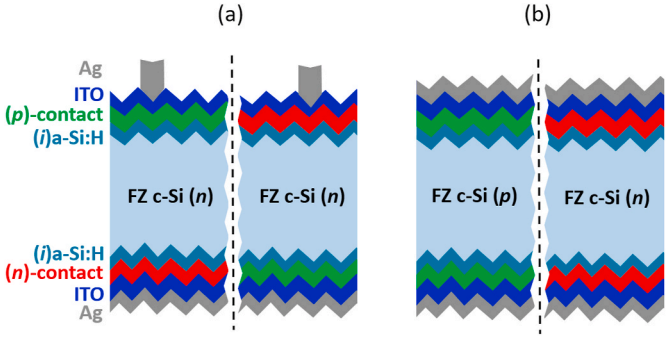

Fig. 3. Schematic sketches of (a) the front and rear junction solar cells under study; (b) symmetrical samples for extracting the contact resistivity ρ_c of doped contact stacks that originate from solar cells in (a). The (*p*)-contact is represented by the (*p*)nc-SiO$_x$:H + (*p*)nc-Si:H stack, while the (*n*)-contact is represented by either (*n*)a-Si:H or (*n*)nc-SiO$_x$:H, as discussed in our previous study [28]. Note that for symmetrical samples in (b) we used either (*p*)- or (*n*)-type c-Si bulk for studying the (*p*)- or (*n*)-contact stacks, respectively.

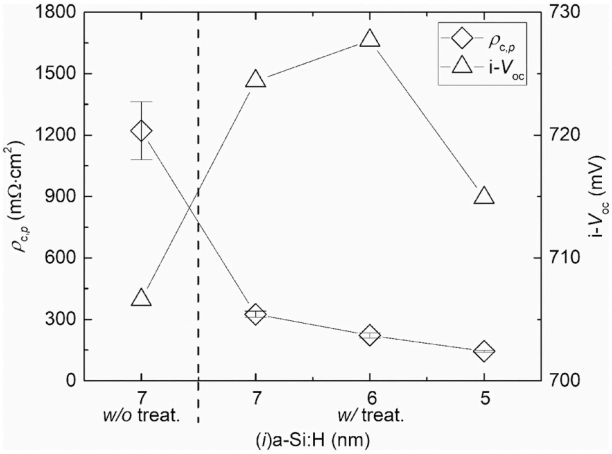

Fig. 4. The contact resistivity $\rho_{c,p}$ and i-V_{oc} of (p)-contact stacks without and with HPT + VHF (i)nc-Si:H interface treatment, and depending on the (i)a-Si:H layer thickness. The passivation quality of the symmetrical test samples was measured before ITO sputtering. The results present averaged $\rho_{c,p}$ from two symmetrical samples and the error bars represent the standard deviations.

enhancement of the selectivity for hole transport. This beneficial effect on $\rho_{c,p}$ is consistent with the reduced E_a of the (p)-contact [10] as is shown in Fig. 2. Furthermore, the interface treatment boosts the p-type wafer passivation quality, resulting in an i-V_{oc} improvement of 18 mV similarly to what was reported previously for the n-type wafer [28]. By further thinning the (i)a-Si:H layer thickness from 7 nm to 5 nm, the $\rho_{c,p}$ is cut down to 144 mΩ·cm^2, which is lower than the majority of reported values in literature featuring either (p)a-Si:H or (p)nc-Si:H as (p)-contact [30,36,37,39–41,51]. Nevertheless, it is not our intention to pass any unfair argument on the goodness of (p)nc-SiO$_x$:H-based (p)-contact with respect to the (p)a-Si:H contact. Specifically, $\rho_{c,p}$ is reduced more than twice by reducing the thickness of the (i)a-Si:H layer by only 2 nm. This layer is directly beneath the (p)-contact and applying a thinner layer does hardly impact the passivation quality. This observation is in line with the trends that have been reported by Leilaeioun et al. [39] but they used a (p)a-Si:H layer. Indeed as reported by others [51–53], thinner (i)a-Si:H may improve the carrier collections through increased carrier tunneling probability. Within this series, 6-nm thick (i)a-Si:H delivers the highest i-V_{oc} of 728 mV and a relatively low $\rho_{c,p}$ of 222 mΩ·cm^2. Thus we implement this (i)a-Si:H layer thickness together with the interface treatment in the samples that will be discussed in the following sections.

3.2.2. *Effect of (p)nc-SiO$_x$:H optoelectrical properties on contact resistivity*

To maximize the $V_{bi,p}$ at the c-Si/(i)a-Si:H interface and, thus, the hole accumulation at the c-Si/(i)a-Si:H interface [10], we applied (p)nc-SiO$_x$:H with a varying difference between E_{04} and E_a by varying the deposition pressure as given in Table 1, where E_{04} is considered as an indication of the layer's mobility gap (E_g) [54]. Here, we compare symmetrical test samples, which feature 4-nm thick (p)nc-SiO$_x$:H deposited after the optimized interface treatment and coated with a 12-nm (p)nc-Si:H layer. To extract the E_a and E_{04} of the three different (p)nc-SiO$_x$:H layers, slightly different from the structure used in Fig. 2, we deposited 20-nm thick (p)nc-SiO$_x$:H layers on glass substrates without (i)a-Si:H coating. The measured E_a and E_{04} of (p)nc-SiO$_x$:H layers are given in Table 2 and indicated as Type-a, Type-b, and Type-c. Then, we evaluated the precursor i-V_{oc} before ITO sputtering and $\rho_{c,p}$ of the symmetrical test samples endowed with (p)nc-SiO$_x$:H layers featuring various E_{04} - E_a values (see Fig. 5).

As illustrated in Fig. 5, by widening the E_{04} - E_a difference from Type-a to Type-b (from 1.870 eV to 2.007 eV), $\rho_{c,p}$ of the (p)-contact stacks significantly drops. Its value is reduced from 1027 mΩ·cm^2 to 307 mΩ·cm^2. We ascribe the reduction of $\rho_{c,p}$ by using Type-b (p)nc-SiO$_x$:H layer to the improved $V_{bi,p}$, which indicates an enhanced band bending

Table 2
The optoelectrical properties of three types of (p)nc-SiO$_x$:H layers.

(p)nc-SiO$_x$:H	Deposition pressure (mbar)	E_{04} (eV)	E_a (meV)	$E_{04} - E_a$ (eV)
Type-a	3.0	2.19	320	1.870
Type-b	2.2	2.36	353	2.007
Type-c	1.4	2.51	424	2.086

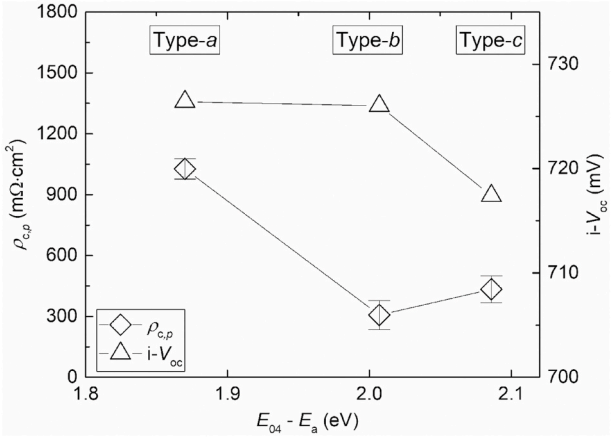

Fig. 5. The contact resistivity $\rho_{c,p}$ and i-V_{oc} of (p)-contact stacks with (p)nc-SiO$_x$:H layers featuring various E_{04} - E_a. The passivation quality of the symmetrical test samples was measured before ITO sputtering. The results present averaged $\rho_{c,p}$ from two symmetrical samples and the error bars represent the standard deviations.

at the c-Si/(i)a-Si:H interface and therefore an increased hole accumulation [10]. By using Type-c (p)nc-SiO$_x$:H layer, which features much higher E_a and E_{04} - E_a as compared to that of Type-a (p)nc-SiO$_x$:H layer, the $\rho_{c,p}$ of the contact stacks is also significantly reduced. A degradation in i-V_{oc} is observed for the sample with Type-c (p)nc-SiO$_x$:H as compared to samples with Type-a and Type-b (p)nc-SiO$_x$:H. We ascribe this to the loss in chemical passivation of (i)a-Si:H, which is sensitive to the varied plasma conditions for realizing the optoelectrical properties of Type-c (p)nc-SiO$_x$:H. Therefore, considering both passivation quality and electrical behavior, Type-b (p)nc-SiO$_x$:H is preferred for solar cells fabrication.

3.2.3. *Effect of thickness combinations of the bi-layer (p)-contact on contact resistivity*

Aside from building up a sufficient $V_{bi,p}$ at the c-Si/(i)a-Si:H interface, a low E_a (p)-contact is critical for achieving an effective transport of positive charges from the (p)-contact to the ITO. As known from the thickness-dependent E_a of (p)-contact discussed in Section 3.1, we tuned the E_a of the (p)-contact via varying the thickness combinations between (p)nc-SiO$_x$:H and (p)nc-Si:H. In Fig. 6 we present their influence on $\rho_{c,p}$ of the symmetrical test samples.

As can be seen in Fig. 6, we observe that the average $\rho_{c,p}$ decreases to a minimum of 291 mΩ·cm^2 with increasing thickness fraction of (p)nc-Si:H. The $\rho_{c,p}$ reduction can be explained by the thickness-dependent E_a of the (p)-contact (see Fig. 2). Indeed, by lowering E_a not only the band bending at the c-Si/(i)a-Si:H interface enhances, but also the potential barrier for holes decreases [10]. Both effects contribute to a more efficient transport of carriers from c-Si to ITO. This also explains the enhanced i-V_{oc} up to 726 mV by increasing the (p)nc-Si:H thickness. It is worth noting that in the absence of (p)nc-Si:H (20 + 0 nm) beneath the ITO layer, we observe a diode behavior of the test sample. We ascribe this to an excessively large transport barrier at the (p)-contact/ITO interface possibly due to a parasitic junction in our 20-nm thick (p)nc-SiO$_x$:H. Further, the complete removal of the (p)nc-SiO$_x$:H (0 + 15

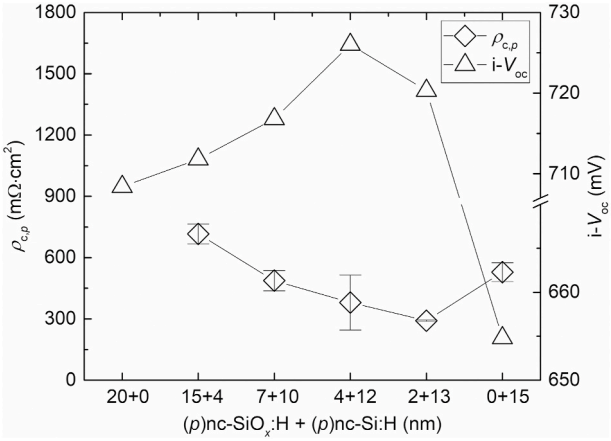

Fig. 6. The contact resistivity $\rho_{c,p}$ and i-V_{oc} of (*p*)-contact stacks with varying (*p*)nc-SiO$_x$:H and (*p*)nc-Si:H layer thicknesses. The passivation quality of the symmetrical test samples was measured before ITO sputtering. The results present averaged $\rho_{c,p}$ from two symmetrical samples and the error bars represent the standard deviations.

nm) results in an i-V_{oc} of only 655 mV, which indicates a very defective c-Si/(*i*)a-Si:H interface. In return, this defective interface might also negatively affect the $\rho_{c,p}$ of the contact stacks. Therefore, the best thickness combination in terms of both i-V_{oc} and $\rho_{c,p}$ is found for the stack with 4 nm (*p*)nc-SiO$_x$:H + 12 nm (*p*)nc-Si:H. The presence of a 4 nm thick (*p*)nc-SiO$_x$:H layer not only guarantees an excellent passivation quality but also enhances the band bending at c-Si/(*i*)a-Si:H interface.

To sum up, we found that the application of the interface treatment together with a thinner (*i*)a-Si:H layer is crucial to minimize the carrier transport losses ($\rho_{c,p}$) in the (*p*)-contact stacks. We also observed (*p*)nc-SiO$_x$:H with a larger E_{04} - E_a difference is critical for a significant reduction of $\rho_{c,p}$. Lastly, a bi-layer (*p*)-contact with thicker (*p*)nc-Si:H tends to deliver a lower $\rho_{c,p}$.

3.3. Solar cells

The studies about resistivity of (*p*)-contact stacks reveal various possible approaches to reduce the $\rho_{c,p}$ by improving hole selectivity and minimizing the transport losses of holes. Accordingly, we implemented the results of the test structures in both front and rear junction solar cells to analyze their resistivity and performance (see Fig. 3(a)). To this purpose, we firstly extracted the solar cell's *pFF* via Suns-V$_{OC}$ measurement and then used the *pFF* to evaluate the solar cell's $R_{s,SunsVoc}$ (mΩ·cm^2) [47,55,56].

3.3.1. Effect of the interface treatment and (i)a-Si:H layer thickness on cell performances

We fabricated front junction solar cells that feature an (*n*)a-Si:H as (*n*)-contact at the rear side, while varying the interface treatment and (*i*)a-Si:H layer thickness before the deposition of the front (*p*)-contact stack (4 nm (*p*)nc-SiO$_x$:H + 16 nm (*p*)nc-Si:H). Solar cells' performance key metrics (V_{oc}, *FF, pFF* and $R_{s,SunsVoc}$) are depicted in Fig. 7.

As shown in Fig. 7, the treatment boosts the average *FF* from 70.9% to 77.0% corresponding to a halved $R_{s,SunsVoc}$ from 2920 mΩ·cm^2 to 1440 mΩ·cm^2. This reduction in $R_{s,SunsVoc}$ is expected from the previous contact resistivity study discussed in Fig. 4, where we observe a more-than-twice reduction in the $\rho_{c,p}$ of the (*p*)-contact stacks by applying the interface treatment. By reducing the thickness of the (*i*)a-Si:H layer beneath the (*p*)-contact from 7 to 5 nm, we observe a 2.3%$_{abs}$ *FF* gain without significant loss in V_{oc}. Accordingly, the average $R_{s,SunsVoc}$ reduces from 1440 mΩ·cm^2 to 930 mΩ·cm^2. Therefore, (*i*)a-Si:H with a thickness of around 5–6 nm is promising to improve the device *FF* while preserving V_{oc}.

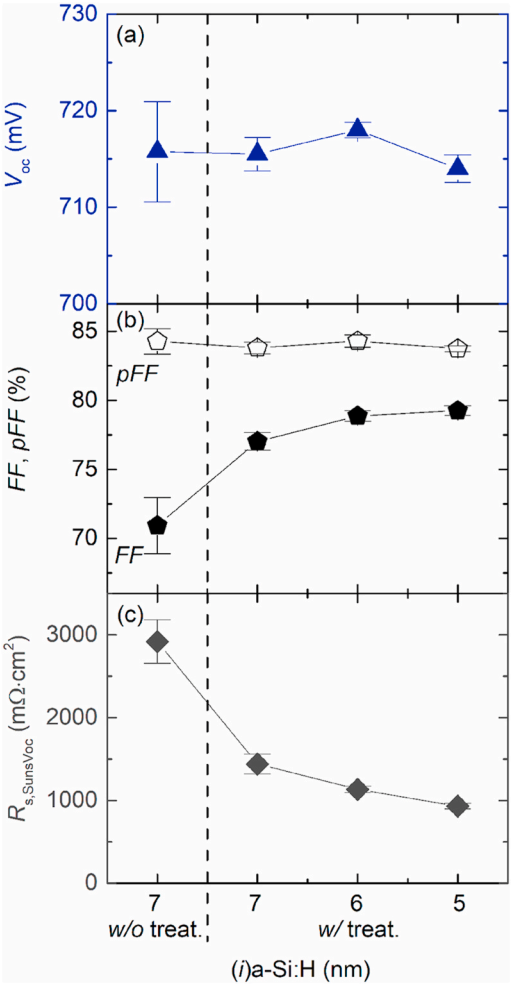

Fig. 7. Front junction FBC-SHJ solar cells processed without and with HPT + VHF (*i*)nc-Si:H interface treatment with varying thicknesses of (*i*)a-Si:H beneath the (*p*)-contact (4 nm (*p*)nc-SiO$_x$:H + 16 nm (*p*)nc-Si:H): (a) V_{oc}; (b) *FF* and *pFF*; (c) $R_{s,SunsVoc}$. Solar cells feature a nominal 3.2% front metal coverage. The results present averaged parameters from four solar cells (the sample with 5 nm (*i*)a-Si:H represents the results of two cells). The error bars represent the standard deviations.

3.3.2. Effect of (p)nc-SiO$_x$:H optoelectrical properties on cell performances

In Fig. 8, we present the effect of (*p*)nc-SiO$_x$:H layers featuring various E_{04} - E_a values on cell parameters of rear junction FBC-SHJ solar cells. These results highlight the effect of E_{04} - E_a on the vertical collections of holes. The thickness of the (*i*)a-Si:H layer under the (*p*)-contact is 6 nm. The front side of the solar cells features an (*n*)a-Si:H layer as (*n*)-contact.

As shown in Fig. 8, we observe a slight decrease of V_{oc} from 720 to 717 mV but an improvement in *FF* from 72.9% to 78.3% with increasing E_{04} - E_a. Correspondingly, the extracted average $R_{s,SunsVoc}$ is observed to be halved from 2002 mΩ·cm^2 down to 972 mΩ·cm^2. Since the (*p*)-contact stacks are placed at the rear side of the solar cells, we can conclude the gain in *FF* mainly comes from the reduced vertical resistance contribution, which originates from decreased $\rho_{c,p}$ of the (*p*)-contact stacks as discussed in Fig. 5.

3.3.3. Effect of thickness combinations of the bi-layer (p)-contact on cell performances

To evaluate the influence of the (*p*)-contact including the different thickness combinations, we compared V_{oc} and *FF* of FBC-SHJ solar cells for the different stacks as mentioned in section 3.2.3. We show results for both front and rear junction configurations (see Figs. 9 and 10,

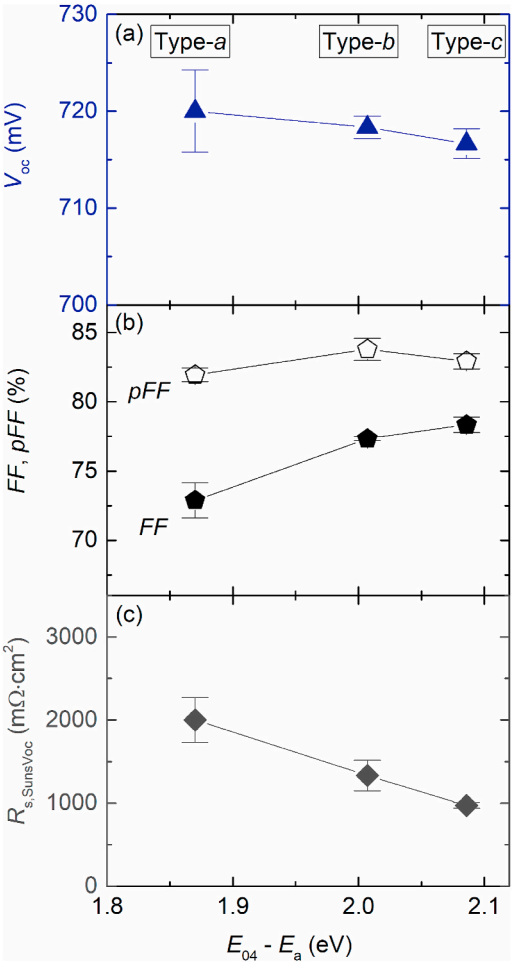

Fig. 8. Rear junction FBC-SHJ solar cells with (*p*)nc-SiO$_x$:H featuring varying E_{04} - E_a in the (*p*)-contact (4 nm (*p*)nc-SiO$_x$:H + 16 nm (*p*)nc-Si:H): (a) V_{oc}; (b) *FF* and *pFF*; (c) $R_{s,SunsVoc}$. Solar cells feature a nominal 4.4% front metal coverage. The results represent averaged parameters from three solar cells (the sample with Type-*a* (*p*)nc-SiO$_x$:H represents the results of two cells). The error bars represent the standard deviations.

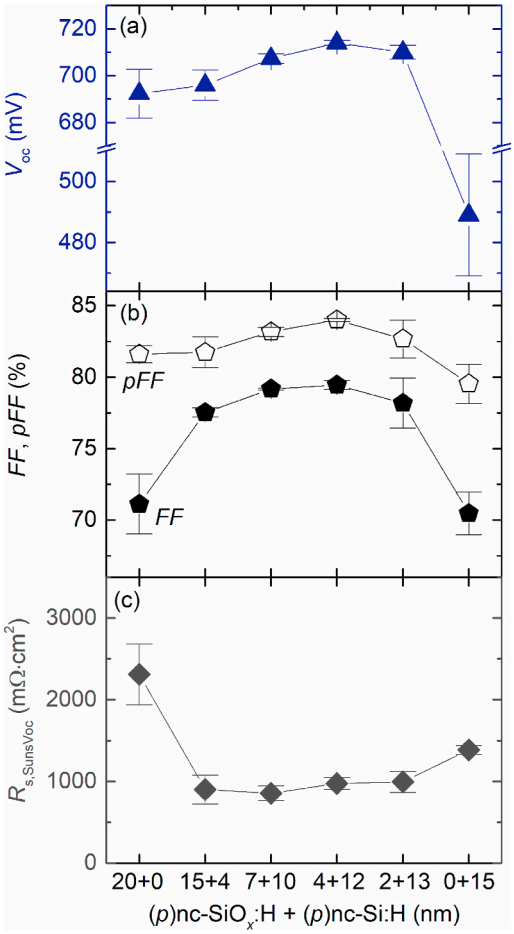

Fig. 9. Front junction FBC-SHJ solar cells with varying thicknesses of (*p*)-contact ((*p*)nc-SiO$_x$:H + (*p*)nc-Si:H): (a) V_{oc}; (b) *FF* and *pFF*; (c) $R_{s,SunsVoc}$. Solar cells feature a nominal 4.4% front metal coverage. The results represent averaged parameters from three solar cells. The error bars represent the standard deviations.

respectively).

In the series of front junction cells, we refer the rear (*n*)-contact to our previously reported (*n*)-contacts based on (*n*)nc-SiO$_x$:H [28]. We observe that V_{oc} and *FF* change simultaneously with increasing the thickness fraction of (*p*)nc-Si:H. The improvement on *FF* observed in solar cells with (*p*)nc-Si:H layers reveals the crucial role of a low E_a layer [28] that is in contact with the ITO. Indeed, *FF* increases by more than 8.5%$_{abs}$ to up to 79.5% by applying the '4 + 12 nm' (*p*)-contact combination. Accordingly, the average $R_{s,SunsVoc}$ also reduces from 2310 mΩ·cm^2 down to 950 mΩ·cm^2 for all cells with a (*p*)-contact including both (*p*)nc-SiO$_x$:H and (*p*)nc-Si:H. Due to the possible aggressive plasma conditions during our (*p*)nc-Si:H deposition, at least 4 nm of (*p*)nc-SiO$_x$:H is again proven to be necessary to preserve the device passivation quality, which also affects the *FF*. In contrast, we also observe an increased average $R_{s,SunsVoc}$ when the cell is poorly passivated.

Lastly, (*p*)-contact stacks with a fixed 4-nm thick (*p*)nc-SiO$_x$:H and with a varying thickness of (*p*)nc-Si:H were applied to rear junction FBC-SHJ solar cells. Device performances are reported in Fig. 10. The front side of the solar cells has an (*n*)a-Si:H layer as the (*n*)-contact.

As illustrated in Fig. 10, we observe a general increment of average V_{oc} and *FF* by increasing the (*p*)nc-Si:H layer thickness. The gains in V_{oc} and *FF* are expected because of the reduced E_a of the (*p*)-contact, supported by the thickness-dependent E_a of (*p*)-contact already shown in Fig. 2. Besides, the absolute gain in *FF* is more pronounced when increasing the (*p*)nc-Si:H layer thickness from 4 nm to 8 nm. We ascribe this to the initial sharp reduction of E_a of the (*p*)-contact when (*p*)nc-Si:H is thinner than 10 nm (see Fig. 2). Further increasing the thickness of the (*p*)nc-Si:H layer results in the gradual saturation of the *FF* around 78.5%. This is also reflected in the evolution of the devices' $R_{s,SunsVoc}$, where the average $R_{s,SunsVoc}$ tends to reach a minimum of 1200 mΩ·cm^2 with the increasing (*p*)nc-Si:H layer thickness.

3.4. Solar cells' resistivity contributions: $R_{s,lateral}$ vs $R_{s,vertical}$

In front junction cells, (*p*)-contact stacks involve not only vertical but also lateral collections of holes. This stimulates our interest in distinguishing the resistance contributions from both directions. To this end, we decomposed the $R_{s,SunsVoc}$ of the abovementioned front junction FBC-SHJ cells with the symmetrical structures as shown in Fig. 3 (b). With the obtained $R_{s,SunsVoc}$, we can derive the lateral $R_{s,lateral}$ that comes from the front side of the solar cells via:

$$R_{s,lateral} = R_{s,SunsVoc} - R_{s,vertical} \quad (3\text{-}3)$$

where:

$$R_{s,vertical} = \left(R_{s,vertical,p} + R_{s,vertical,n}\right)/2 \quad (3\text{–}4)$$

the $R_{s,vertical,p}$ and $R_{s,vertical,n}$ correspond to resistivity contributions from the (*p*)-contact stacks and the (*n*)-contact stacks of the solar cells, respectively. Therefore, aside from the symmetrical (*p*)-contact stacks

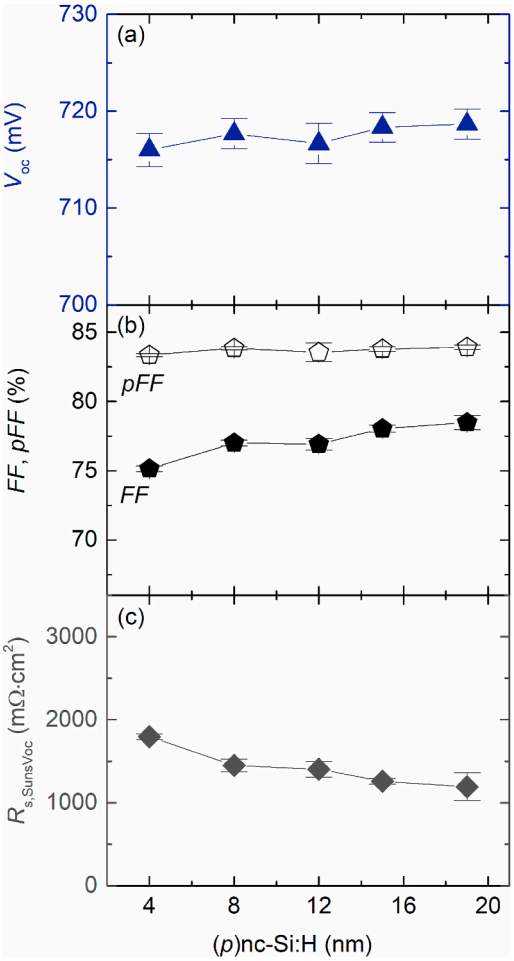

Fig. 10. Rear junction FBC-SHJ solar cells with (*p*)-contacts featuring a fixed 4-nm thick (*p*)nc-SiO$_x$:H but varying (*p*)nc-Si:H layer thicknesses: (a) V_{oc}; (b) *FF* and *pFF*; (c) $R_{s,SunsVoc}$. Solar cells feature a nominal 4.4% metal coverage. The results represent averaged parameters from three solar cells. The error bars represent the standard deviations.

samples already made, we also fabricated symmetrical (*n*)-contact stacks samples, which have the same structures as the corresponding rear (*n*)-contact stacks in the solar cells (see Fig. 3(b)). Here, we consider only vertical transport of electrons through the rear (*n*)-contact stacks.

The breakdown of solar cells' $R_{s,SunsVoc}$ for different layers and treatments is illustrated in Fig. 11.

As it can be seen from the analysis of $R_{s,SunsVoc}$ in Fig. 11(a) and (b), the variations in $\rho_{c,p}$ of the (*p*)-contact stacks (see Section 3.2) do not only change directly the $R_{s,vertical,p}$ but also the distribution of the $R_{s,lateral}$. In Fig. 11(a), the (*n*)a-Si:H based (*n*)-contact stacks account for an $R_{s,vertical,n}$ of 102 mΩ·cm^2 ($\rho_{c,n}$ of 63 mΩ·cm^2), which is less resistive than (*p*)-contact stacks. When applying the interface treatment, we observe a significant reduction in $R_{s,vertical,p}$ as a result of the decrement of $\rho_{c,p}$ of the (*p*)-contact stacks. Meanwhile, we also recognize a lower contribution from $R_{s,lateral}$. The reduction of $R_{s,lateral}$ may result from both stronger band bending and better collection of holes from (*p*)-contact to the ITO layer. Moreover, thinning down the (*i*)a-Si:H beneath the (*p*)-contact also follows the trends but with rather comparable reductions of both $R_{s,vertical,p}$ and $R_{s,lateral}$. In fact, (*p*)-contact stacks with thinner (*i*)a-Si:H layer features lower vertical resistance, which promotes lateral transport through ITO, thus a lower $R_{s,lateral}$ as well.

In Fig. 11(b), it is shown that the contribution of the (*n*)-contact stack based on (*n*)nc-SiO$_x$:H to $R_{s,vertical,n}$ is 71 mΩ·cm^2 ($\rho_{c,n}$ of 33 mΩ·cm^2). Differently, by varying thickness combinations of the (*p*)-contact, we observe a trade-off between $R_{s,vertical,p}$ and $R_{s,lateral}$. Due to the observed diode behavior of the symmetrical sample (see Fig. 6) with only (*p*)nc-SiO$_x$:H (20 + 0 nm), we present only its device $R_{s,SunsVoc}$, which is the most resistive within the series. Along with the increased fraction of (*p*) nc-Si:H layer, we observe the gradual lowering of $R_{s,vertical}$ because of the reduced $\rho_{c,p}$ of the (*p*)-contact stacks (see Fig. 6). However, the increased contribution from $R_{s,lateral}$ compensates the reduced $R_{s,vertical}$, thus maintaining the devices' $R_{s,SunsVoc}$ nearly constant. We ascribe this to competing effects between the ones on carrier collections due to thinner (*p*)nc-SiO$_x$:H and thicker (*p*)nc-Si:H. It is worth noting that a thicker (*p*) nc-SiO$_x$:H or (*p*)nc-Si:H tends to enhance the band bending inside (*n*)c-Si as a result of thickness-dependent E_a of (*p*)-contact, thus reducing $\rho_{c,p}$ and promoting the lateral transport inside ITO for both cases. Therefore, on the one hand, a thinner (*p*)nc-SiO$_x$:H is less likely to induce an efficient space-charge layer (band bending) inside the (*n*)c-Si bulk as compared to its thicker counterpart. Thus, a thinner (*p*)nc-SiO$_x$:H layer

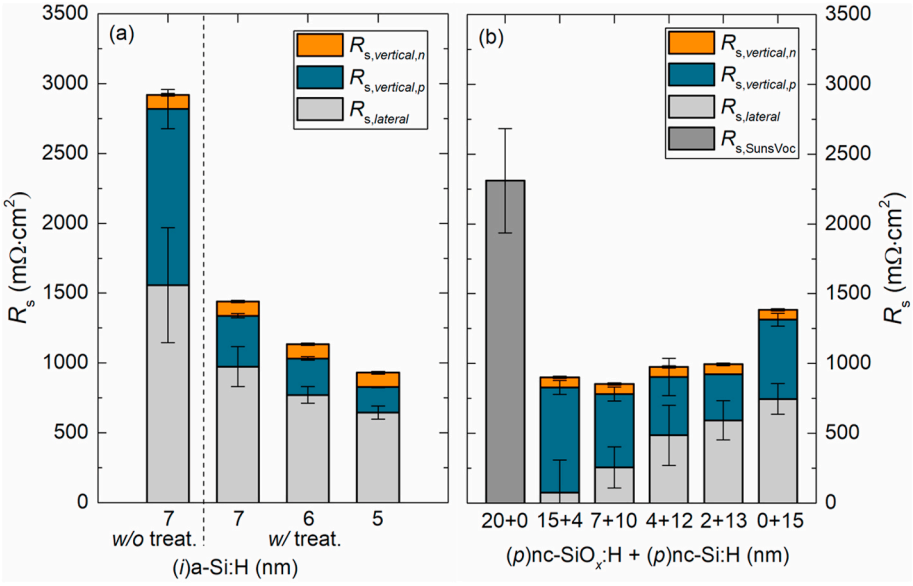

Fig. 11. The decompositions of front junction FBC-SHJ solar cells' $R_{s,SunsVoc}$ with $R_{s,vertical}$ (distinguished between (*n*)-contact stacks $R_{s,vertical,n}$ and (*p*)-contact stacks $R_{s,vertical,p}$) and $R_{s,lateral}$: (a) effect of the interface treatment and (*i*)a-Si:H layer thickness; (b) effect of thickness combinations of the bi-layer (*p*)-contact. The error bars represent the standard deviations.

may require more support for the lateral transport of holes from the space-charge layer inside the (*n*)c-Si bulk. On the other hand, a thicker (*p*)nc-Si:H is capable of reducing the E_a of the (*p*)-contact and thus the $\rho_{c,p}$ and for this reason, a more efficient lateral transport of holes inside the ITO is expected. As it can be seen from Fig. 11(b), the increased $R_{s,lateral}$ with thinner (*p*)nc-SiO$_x$:H and thicker (*p*)nc-Si:H indicates that more holes transport laterally through the (*n*)c-Si bulk. Therefore, there is a more dominating effect of the (*p*)nc-SiO$_x$:H layer thickness on the lateral transport distribution of holes. Besides, similar $R_{s,SunsVoc}$ values with different vertical and lateral components also reveal that $R_{s,SunsVoc}$ is limited by lateral transport in the device ascribed to ITO mobility and front Ag grid pitch size. Lastly, the cell that has only (*p*)nc-Si:H presents both increased $R_{s,vertical}$ and $R_{s,lateral}$ that result from increased $\rho_{c,p}$ and decreased V_{oc}.

To deeper understand the role of the $R_{s,lateral}$ as observed in Fig. 11 (b), we performed TCAD simulations to analyze front junction FBC-SHJ solar cells featuring varied thickness combinations of the bi-layer (*p*)-contact. We evaluated the charge per second that moves laterally in each layer on the front sides of solar cells under maximum power point (MPP) conditions. Since the lateral current flow through the (*p*)-contact is negligible as compared to the one of the c-Si bulk and the ITO layer, we present here only the results of the c-Si bulk and ITO layer. The values are normalized for all samples and are shown in Fig. 12(a). Note, the component that is missing in Fig. 12(a) to reach 100% for each thickness combination indicates non-collected (recombined) carriers as compared to the optimal sample featuring '4 + 12 nm' (*p*)-contact.

As noticeable in Fig. 12(a), the lateral current flow at MPP increases with the thicker (*p*)nc-Si:H (or thinner (*p*)nc-SiO$_x$:H). By lowering the $\rho_{c,p}$ of the (*p*)-contact stacks, the probability of holes to be transported from the c-Si to the ITO increases. Interestingly, with increasing thickness of the (*p*)nc-Si:H layer (or decreasing thickness of (*p*)nc-SiO$_x$:H), we observe variations in the c-Si bulk contribution. Not only the absolute current that is laterally transported through the c-Si bulk increases but also its relative fraction increases. This is evident, especially, by comparing samples with '15 + 4 nm' and '4 + 12 nm' (*p*)-contacts. As expected, these increased c-Si bulk contributions elucidate the higher $R_{s,lateral}$ as observed in Fig. 11(b). Besides, the schematic sketches of lateral current flows in the simulated solar cells are shown in Fig. 12(b) and (c). In fact, from the simulations, the hole concentration (N_h) in the space-charge layer differs by implementing (*p*)-contacts with different thickness combinations. Specifically, the N_h in the space charge layer is around 10^{17} cm^{-3} for the cell with '15 + 4 nm' (*p*)-contact, which is nearly one order of magnitude higher than that of the cell with '2 + 13 nm' (*p*)-contact. This varied N_h in the space-charge layer is reflected in a form of varied space-charge layer thickness as shown in Fig. 12(b) and (c). Although the cell with '15 + 4 nm' (*p*)-contact features a lower $\rho_{c,p}$ as compared to that of the cell with '2 + 13 nm', a stronger band bending induced by the thicker (*p*)nc-SiO$_x$:H promotes the carrier lateral collection through ITO, and vice versa.

With the knowledge of solar cells' performances and during this study further careful processing of the FBC-SHJ solar cells, we present in Fig. 13(a) and (b) the independently certified *J-V* characteristics of our best front and rear junction FBC-SHJ solar cells, respectively. The corresponding decompositions of solar cells's $R_{s,SunsVoc}$ are also presented in Fig. 13. For the front junction cell, we used (*n*)a-Si:H as (*n*)-contact and we implemented the optimized 6 nm (*i*)a-Si:H and '4 + 12 nm' (*p*)-contact together with the interface treatment at the front side. While for the rear junction cell, instead of '4 + 12 nm' (*p*)-contact, we applied '4 + 16 nm' due to less strict optical limitations when the (*p*)-contact is located at the rear side of the solar cell. With these, we have achieved *FF* of 80.9% and 80.4% for front and rear junction configurations, respectively. Moreover, thanks to the more transparent (*n*)-contacts [28] based on (*n*)nc-SiO$_x$:H placed at the sunny side, we achieved an efficiency as high as 22.47% in the rear junction configuration. Lastly, as seen from the decompositions of solar cells' $R_{s,SunsVoc}$, the higher $R_{s,lateral}$ for this rear junction cell indicates that more electrons transport laterally through the (*n*)c-Si bulk as compared to the fraction transporting through the ITO. This corresponds to similar observations as previously reported by Bivour et al. [57].

4. Conclusion

In this work, we investigated and optimized hole collectors – or (*p*)-contact stacks – based on bi-layers of (*p*)nc-SiO$_x$:H and (*p*)nc-Si:H, which are integrated into high-efficiency SHJ solar cells.

We determined the thickness-dependent E_a of the bi-layer (*p*)-contact, for which the thicker the (*p*)nc-Si:H the lower the E_a of the (*p*)-contact. Meanwhile, we demonstrated the necessity of our HPT + VHF (*i*)nc-Si:H interface treatment, which significantly improved the electrical properties of the bi-layer (*p*)-contact, especially when it is thinner than 30 nm overall. Accordingly, the interface treatment also induced significant $\rho_{c,p}$ reduction of the (*p*)-contact stacks. Besides, a thinner (*i*)a-Si:H layer proved to minimize transport losses for holes. We have reported (*p*)-contact stacks featuring a low contact resistance ($\rho_{c,p}$ of 144

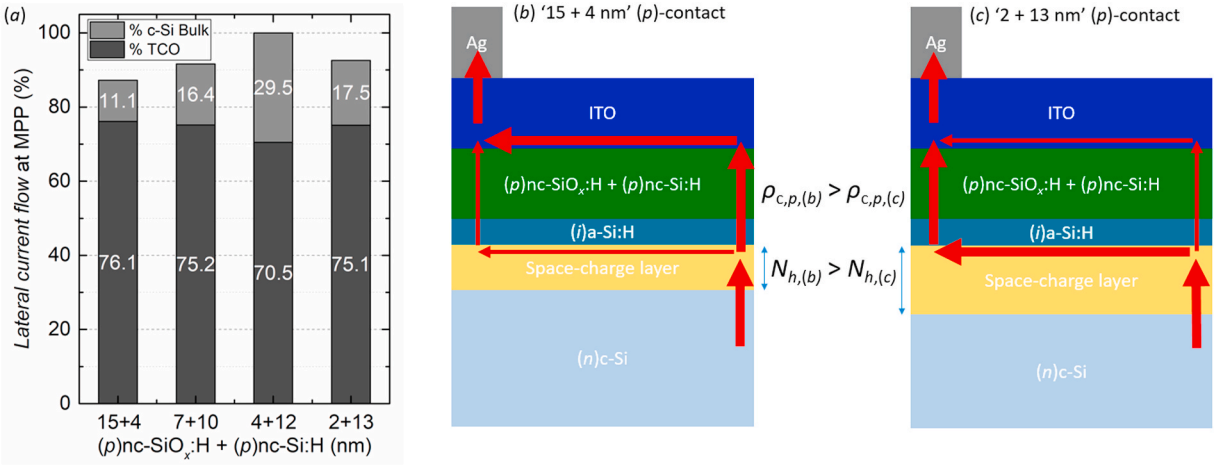

Fig. 12. The (a) simulations and (b), (c) schematic sketches of simulated lateral current flow distributions within the c-Si bulk and ITO layer in front junction FBC-SHJ solar cells with varying thickness combinations of the bi-layer (*p*)-contact. Note, the component that is missing in (a) to reach 100% for each thickness combination indicates non-collected (recombined) carriers as compared to the optimal sample featuring '4 + 12 nm' (*p*)-contact. The $\rho_{c,p,(b)}$ and $\rho_{c,p,(c)}$ represent the contact resistivity of the contact stacks featuring '15 + 4 nm' and '2 + 13 nm' (*p*)-contact, respectively. $N_{h,(b)}$ and $N_{h,(c)}$ are the hole concentration in the space-charge layer of (*n*)c-Si for cells featuring '15 + 4 nm' and '2 + 13 nm' (*p*)-contact, respectively.

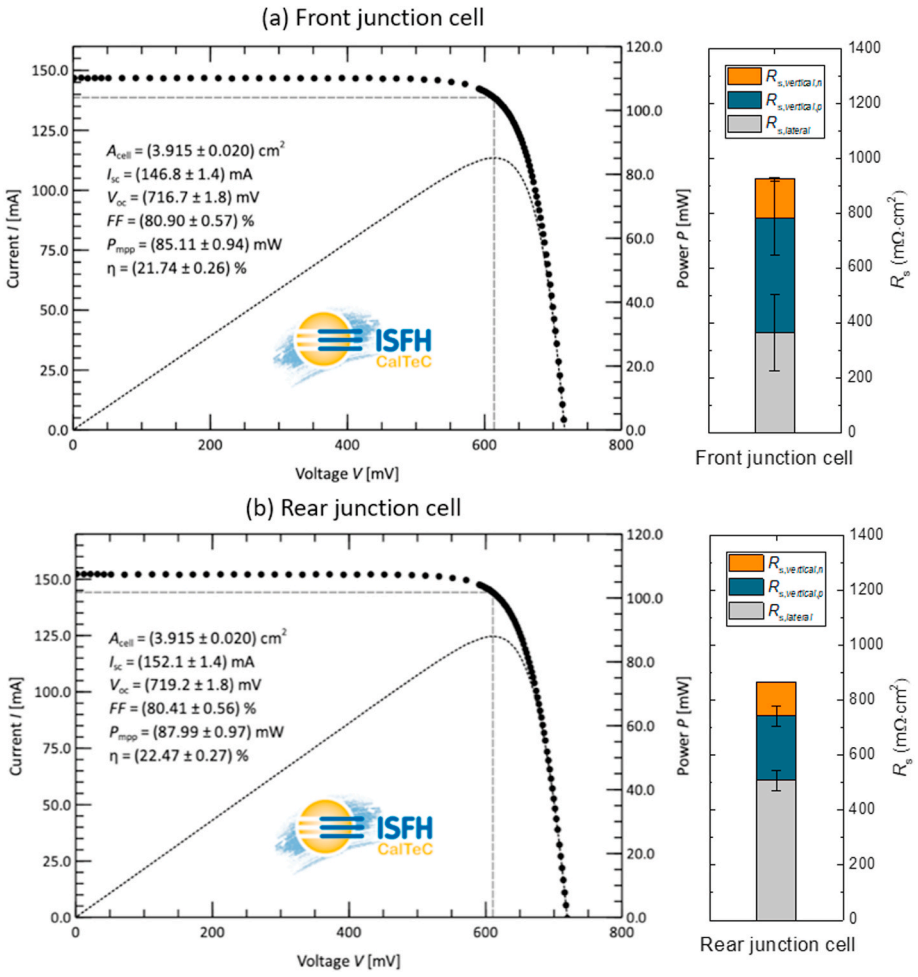

Fig. 13. The independently certified *I–V* characteristics and device parameters of the best (a) front junction and (b) rear junction FBC-SHJ solar cells. The corresponding decompositions of solar cells' $R_{s,SunsVoc}$ are also presented. The *J-V* characteristics certifications were performed at ISFH CalTeC (Germany).

mΩ·cm^2) when (*i*)a-Si:H is 5 nm. Interestingly, (*p*)nc-SiO$_x$:H layers featuring a larger E_{04} - E_a were found to be beneficial for the $\rho_{c,p}$. Moreover, by varying the thickness combinations in the (*p*)nc-SiO$_x$:H and (*p*)nc-Si:H stacks, we were able to prove the critical roles of both (*p*) nc-SiO$_x$:H and (*p*)nc-Si:H. In particular, (*p*)nc-SiO$_x$:H preserves the passivation quality and enables sufficient band bending at c-Si/(*i*)a-Si:H interface, while (*p*)nc-Si:H enhances the transport of holes to ITO and the band bending as well.

Subsequently, we have observed that the evolution of solar cells' *FF* are closely correlated to their $R_{s,SunsVoc}$ and therefore to the $\rho_{c,p}$ of (*p*)-contact stacks. It is worth noting that in front junction FBC-SHJ solar cells, $\rho_{c,p}$ of (*p*)-contact stacks also affects the distribution of vertical and lateral transport of holes. The application of an interface treatment and a thinner (*i*)a-Si:H layer reduced both vertical and lateral resistance losses at the same time. Differently, we have observed a trade-off between vertical and lateral resistance when we varied the thickness combinations of the (*p*)-contact. The latter finding was supported by TCAD simulation, from which we observed increased contributions from the space-charge layer inside the (*n*)c-Si bulk when a thinner (*p*)nc-SiO$_x$:H is applied. Our best cells were certified to feature *FF* well-above 80% for both front and rear configurations, and an efficiency of 22.47% was achieved for a rear junction solar cell.

CRediT authorship contribution statement

Yifeng Zhao: Conceptualization, Methodology, Investigation, Validation, Formal analysis, Visualization, Writing - original draft. **Paul Procel:** Conceptualization, Methodology, Software, Writing - review & editing. **Can Han:** Methodology, Writing - review & editing. **Luana Mazzarella:** Writing - review & editing, Supervision. **Guangtao Yang:** Writing - review & editing. **Arthur Weeber:** Writing - review & editing, Supervision. **Miro Zeman:** Supervision, Project administration, Funding acquisition. **Olindo Isabella:** Writing - review & editing, Supervision.

Declaration of competing interest

The authors declare that they have no known competing financial interests or personal relationships that could have appeared to influence the work reported in this paper.

Acknowledgment

This study receives financial support from the NWO Joint Solar Program III (680-91-011) and technical support from PVMD group technicians Martijn Tijssen and Stefaan Heirman.

References

[1] D. Adachi, J.L. Hernández, K. Yamamoto, Impact of carrier recombination on fill factor for large area heterojunction crystalline silicon solar cell with 25.1% efficiency, Appl. Phys. Lett. 107 (2015) 233506.
[2] Z.C. Holman, A. Descoeudres, L. Barraud, F.Z. Fernandez, J.P. Seif, S. De Wolf, C. Ballif, Current losses at the front of silicon heterojunction solar cells, IEEE J. Photovolt. 2 (2012) 7–15.
[3] W.E. Spear, P.G. Le Comber, Substitutional doping of amorhous silicon, Solid State Commun. 17 (1975) 1193–1196.

[4] W. Rehm, R. Fischer, J. Stuke, H. Wagner, Photo and dark conductivity of doped amorphous silicon, Phys. Status Solidi 79 (1977) 539–547.
[5] S.G. Greenbaum, W.E. Carlos, P.C. Taylor, Local bonding arrangements of boron in doped hydrogenated amorphous silicon, J. Appl. Phys. 56 (1984) 1874–1877.
[6] S. De Wolf, M. Kondo, Boron-doped a-Si:H/c-Si interface passivation: degradation mechanism, Appl. Phys. Lett. 91 (2007) 112109.
[7] S.M. De Nicolás, D. Muñoz, A.S. Ozanne, N. Nguyen, P.J. Ribeyron, Optimisation of doped amorphous silicon layers applied to heterojunction solar cells, Energy Procedia 8 (2011) 226–231.
[8] R. Rößler, C. Leendertz, L. Korte, N. Mingirulli, B. Rech, Impact of the transparent conductive oxide work function on injection-dependent a-Si: H/c-Si band bending and solar cell parameters, J. Appl. Phys. 113 (2013) 144513.
[9] M. Bivour, S. Schröer, M. Hermle, Numerical analysis of electrical TCO/a-Si:H(p) contact properties for silicon heterojunction solar cells, Energy Procedia 38 (2013) 658–669.
[10] P. Procel, G. Yang, O. Isabella, M. Zeman, Theoretical evaluation of contact stack for high efficiency IBC-SHJ solar cells, Sol. Energy Mater. Sol. Cells 186 (2018) 66–77.
[11] P. Procel, H. Xu, A. Saez, C. Ruiz-Tobon, L. Mazzarella, Y. Zhao, C. Han, G. Yang, M. Zeman, O. Isabella, The role of heterointerfaces and subgap energy states on transport mechanisms in silicon heterojunction solar cells, Prog. Photovoltaics Res. Appl. 28 (2020) 935–945.
[12] J. Temmler, M. Bivour, H. Steinkemper, M. Hermle, Boron doped a-SiC: H front layers for silicon heterojunction cells, Proc. 29th Euro. Photovolt. Sol. Energy Conf. Exhib. (2014) 481–483.
[13] J. Sritharathikhun, H. Yamamoto, S. Miyajima, A. Yamada, M. Konagai, Optimization of amorphous silicon oxide buffer layer for high-efficiency p-type hydrogenated microcrystalline silicon oxide/n-type crystalline silicon heterojunction solar cells, Jpn. J. Appl. Phys. 47 (2008) 8452.
[14] J. Sritharathikhun, F. Jiang, S. Miyajima, A. Yamada, M. Konagai, Optimization of p-type hydrogenated microcrystalline silicon oxide window layer for high-efficiency crystalline silicon heterojunction solar cells, Jpn. J. Appl. Phys. 48 (2009) 101603.
[15] K. Ding, U. Aeberhard, F. Finger, U. Rau, Silicon heterojunction solar cell with amorphous silicon oxide buffer and microcrystalline silicon oxide contact layers, Phys. Status Solidi Rapid Res. Lett. 6 (2012) 193–195.
[16] P. Cuony, D.T.L. Alexander, I. Perez-Wurfl, M. Despeisse, G. Bugnon, M. Boccard, T. Söderström, A. Hessler-Wyser, C. Hébert, C. Ballif, Silicon filaments in silicon oxide for next-generation photovoltaics, Adv. Mater. 24 (2012) 1182–1186.
[17] K. Nakada, S. Miyajima, M. Konagai, Application of n-type microcrystalline silicon oxide as back reflector of crystalline silicon heterojunction solar cells, Jpn. J. Appl. Phys. 54 (2015) 82301.
[18] S. Kirner, L. Mazzarella, L. Korte, B. Stannowski, B. Rech, R. Schlatmann, Silicon heterojunction solar cells with nanocrystalline silicon oxide emitter: insights into charge carrier transport, IEEE J. Photovolt. 5 (2015) 1601–1605.
[19] L. Mazzarella, S. Kirner, B. Stannowski, L. Korte, B. Rech, R. Schlatmann, L. Mazzarella, S. Kirner, B. Stannowski, L. Korte, B. Rech, R. Schlatmann, p-type microcrystalline silicon oxide emitter for silicon heterojunction solar cells allowing current densities above 40 mA/cm2, Appl. Phys. Lett. 106 (2015), 023902.
[20] S. Dhar, S. Mandal, G. Das, S. Mukhopadhyay, P.P. Ray, C. Banerjee, A.K. Barua, Silicon heterojunction solar cells with novel fluorinated n-type nanocrystalline silicon oxide emitters on p-type crystalline silicon, Jpn. J. Appl. Phys. 54 (2015), 08KD03.
[21] J. Stuckelberger, G. Nogay, P. Wyss, Q. Jeangros, C. Allebé, F. Debrot, X. Niquille, M. Ledinsky, A. Fejfar, M. Despeisse, F.-J. Haug, P. Löper, C. Ballif, Passivating electron contact based on highly crystalline nanostructured silicon oxide layers for silicon solar cells, Sol. Energy Mater. Sol. Cells 158 (2016) 2–10.
[22] H.A. Gatz, J.K. Rath, M.A. Verheijen, W.M.M. Kessels, R.E.I. Schropp, Silicon heterojunction solar cell passivation in combination with nanocrystalline silicon oxide emitters, Phys. Status Solidi 213 (2016) 1932–1936.
[23] L. Mazzarella, A.B. Morales-Vilches, M. Hendrichs, S. Kirner, L. Korte, R. Schlatmann, B. Stannowski, Nanocrystalline n-type silicon oxide front contacts for silicon heterojunction solar cells: photocurrent enhancement on planar and textured substrates, IEEE J. Photovolt. 8 (2017) 70–78.
[24] L. Mazzarella, A.B. Morales-Vilches, L. Korte, R. Schlatmann, B. Stannowski, Ultra-thin nanocrystalline n-type silicon oxide front contact layers for rear-emitter silicon heterojunction solar cells, Sol. Energy Mater. Sol. Cells 179 (2018) 386–391.
[25] J. Haschke, R. Monnard, L. Antognini, J. Cattin, A.A. Abdallah, B. Aïssa, M. M. Kivambe, N. Tabet, M. Boccard, C. Ballif, Nanocrystalline silicon oxide stacks for silicon heterojunction solar cells for hot climates, AIP Conf. Proc. 1999 (2018) 30001.
[26] A. Richter, V. Smirnov, A. Lambertz, K. Nomoto, K. Welter, K. Ding, Versatility of doped nanocrystalline silicon oxide for applications in silicon thin-film and heterojunction solar cells, Sol. Energy Mater. Sol. Cells 174 (2018) 196–201.
[27] D. Qiu, W. Duan, A. Lambertz, K. Bittkau, P. Steuter, Y. Liu, A. Gad, M. Pomaska, U. Rau, K. Ding, Front contact optimization for rear-junction SHJ solar cells with ultra-thin n-type nanocrystalline silicon oxide, Sol. Energy Mater. Sol. Cells 209 (2020) 110471.
[28] Y. Zhao, L. Mazzarella, P. Procel, C. Han, G. Yang, A. Weeber, M. Zeman, O. Isabella, Doped hydrogenated nanocrystalline silicon oxide layers for high-efficiency c-Si heterojunction solar cells, Prog. Photovoltaics Res. Appl. 28 (2020) 425–435.
[29] C. Lei, C.-W. Peng, J. Zhong, H. Li, M. Yang, K. Zheng, X. Qu, C. Yu, Y. Li, X. Xu, Phosphorus treatment to promote crystallinity of the microcrystalline silicon front contact layers for highly efficient heterojunction solar cells, Sol. Energy Mater. Sol. Cells 209 (2020) 110439.
[30] G. Nogay, J.P. Seif, Y. Riesen, A. Tomasi, Q. Jeangros, N. Wyrsch, F.-J. Haug, S. De Wolf, C. Ballif, Nanocrystalline silicon carrier collectors for silicon heterojunction solar cells and impact on low-temperature device characteristics, IEEE J. Photovolt. 6 (2016) 1654–1662.
[31] P. Roca i Cabarrocas, N. Layadi, T. Heitz, B. Drévillon, I. Solomon, Substrate selectivity in the formation of microcrystalline silicon: mechanisms and technological consequences, Appl. Phys. Lett. 66 (1995) 3609–3611.
[32] R.J. Handy, Theoretical analysis of the series resistance of a solar cell, Solid State Electron. 10 (1967) 765–775.
[33] D.K. Schroder, D.L. Meier, Solar cell contact resistance—a review, IEEE Trans. Electron. Dev. 31 (1984) 637–647.
[34] D.L. Meier, D.K. Schroder, Contact resistance: its measurement and relative importance to power loss in a solar cell, IEEE Trans. Electron. Dev. 31 (1984) 647–653.
[35] A. Cruz, E.-C. Wang, A.B. Morales-Vilches, D. Meza, S. Neubert, B. Szyszka, R. Schlatmann, B. Stannowski, Effect of front TCO on the performance of rear-junction silicon heterojunction solar cells: insights from simulations and experiments, Sol. Energy Mater. Sol. Cells 195 (2019) 339–345.
[36] S.Y. Lee, H. Choi, H. Li, K. Ji, S. Nam, J. Choi, S.W. Ahn, H.M. Lee, B. Park, Analysis of a-Si:H/TCO contact resistance for the Si heterojunction back-contact solar cell, Sol. Energy Mater. Sol. Cells 120 (2014) 412–416.
[37] D. Lachenal, D. Baetzner, W. Frammelsberger, B. Legradic, J. Meixenberger, P. Papet, B. Strahm, G. Wahli, Heterojunction and passivated contacts: a simple method to extract both n/tco and p/tco contacts resistivity, Energy Procedia 92 (2016) 932–938.
[38] R. Gogolin, M. Turcu, R. Ferr, J. Clemens, N. Harder, R. Brendel, J. Schmidt, Analysis of series resistance losses in a -Si:H/c-Si heterojunction solar cells, IEEE J. Photovolt. 4 (2018) 1169–1176.
[39] M.A. Leilaeioun, W. Weigand, M. Boccard, J.Y. Zhengshan, K. Fisher, Z.C. Holman, Contact resistivity of the p-type amorphous silicon hole contact in silicon heterojunction solar cells, IEEE J. Photovolt. 10 (2019) 54–62.
[40] C. Messmer, M. Bivour, C. Luderer, L. Tutsch, J. Schön, M. Hermle, Influence of interfacial oxides at TCO/doped Si thin film contacts on the charge carrier transport of passivating contacts, IEEE J. Photovolt. 10 (2020) 343–350.
[41] P. Procel, H. Xu, L.L. Senaud, B. Paviet-Salomon, H.S. Radhakrishnan, M. Filipič, M. Xu, M. Boccard, A. Fioretti, R. Monnard, J.-C. Stang, P. Wagner, D. Meza, D. Lachenal, B. Strahm, W. Duang, A. Lambertz, A. Fejfar, K. Ding, M. Despeisse, I. Gordon, L. Korte, C. Ballif, O. Isabella, M. Zeman, On the correlation between contact resistivity and high efficiency in (IBC-) SHJ solar cells, in: Proc. 36th Eur. Photovolt. Sol. Energy Conf. Exhib., Marsella, 2019, pp. 251–254.
[42] J.A. Sap, O. Isabella, K. Jäger, M. Zeman, Extraction of optical properties of flat and surface-textured transparent conductive oxide films in a broad wavelength range, Thin Solid Films 520 (2011) 1096–1101.
[43] WTheiss hardware and software, SCOUT, accessed, https://www.wtheiss.com/. (Accessed 23 July 2019).
[44] C. Han, G. Yang, A. Montes, P. Procel, L. Mazzarella, Y. Zhao, S. Eijt, H. Schut, X. Zhang, M. Zeman, O. Isabella, Realizing the potential of RF-sputtered hydrogenated fluorine-doped indium oxide as electrode materials for ultrathin SiOx/poly-Si passivating contacts, ACS Appl. Energy Mater. (2020) in press.
[45] G. Yang, P. Guo, P. Procel, G. Limodio, A. Weeber, O. Isabella, M. Zeman, High-efficiency black IBC c-Si solar cells with poly-Si as carrier-selective passivating contacts, Sol. Energy Mater. Sol. Cells 186 (2018) 9–13.
[46] D. Deligiannis, S. Alivizatos, A. Ingenito, D. Zhang, M. van Sebille, R.A.C.M.M. van Swaaij, M. Zeman, Wet-chemical treatment for improved surface passivation of textured silicon heterojunction solar cells, Energy Procedia 55 (2014) 197–202.
[47] R.A. Sinton, A. Cuevas, Contactless determination of current–voltage characteristics and minority-carrier lifetimes in semiconductors from quasi-steady-state photoconductance data, Appl. Phys. Lett. 69 (1996) 2510–2512.
[48] M.J. Kerr, A. Cuevas, R.A. Sinton, Generalized analysis of quasi-steady-state and transient decay open circuit voltage measurements, J. Appl. Phys. 91 (2002) 399–404.
[49] Synopsis, Sentaurus Device User vol. 2009, 2013.
[50] C. Han, L. Mazzarella, Y. Zhao, G. Yang, P. Procel, M. Tijssen, A. Montes, L. Spitaleri, A. Gulino, X. Zhang, O. Isabella, M. Zeman, High-mobility hydrogenated fluorine-doped indium oxide film for passivating contacts c-Si solar cells, ACS Appl. Mater. Interfaces 11 (2019) 45586–45595.
[51] P. Muralidharan, M.A. Leilaeioun, W. Weigand, Z.C. Holman, S.M. Goodnick, D. Vasileska, Understanding transport in hole contacts of silicon heterojunction solar cells by simulating TLM structures, IEEE J. Photovolt. 10 (2020) 363–371.
[52] M.R. Page, E. Iwaniczko, Y.Q. Xu, L. Roybal, F. Hasoon, Q. Wang, R.S. Crandall, Amorphous/crystalline silicon heterojunction solar cells with varying i-layer thickness, Thin Solid Films 519 (2011) 4527–4530.
[53] M. Mikolášek, M. Nemec, M. Vojs, J. Jakabovič, V. Řeháček, D. Zhang, M. Zeman, L. Harmatha, Electrical transport mechanisms in amorphous/crystalline silicon heterojunction: impact of passivation layer thickness, Thin Solid Films 558 (2014) 315–319.
[54] C.R. Wronski, S. Lee, M. Hicks, S. Kumar, Internal photoemission of holes and the mobility gap of hydrogenated amorphous silicon, Phys. Rev. Lett. 63 (1989) 1420.

[55] D. Pysch, A. Mette, S.W. Glunz, A review and comparison of different methods to determine the series resistance of solar cells, Sol. Energy Mater. Sol. Cells 91 (2007) 1698–1706.
[56] F. Feldmann, M. Bivour, C. Reichel, M. Hermle, S.W. Glunz, Passivated rear contacts for high-efficiency n-type Si solar cells providing high interface passivation quality and excellent transport characteristics, Sol. Energy Mater. Sol. Cells 120 (2014) 270–274.
[57] M. Bivour, S. Schröer, M. Hermle, S.W. Glunz, Silicon heterojunction rear emitter solar cells: less restrictions on the optoelectrical properties of front side TCOs, Sol. Energy Mater. Sol. Cells 122 (2014) 120–129.